ORIGINAL PAPER

Image filtering for two-photon deep imaging of lymphonodes

**Michele Caccia · Laura Sironi · Maddalena Collini ·
Giuseppe Chirico · Ivan Zanoni · Francesca Granucci**

Abstract Non-linear excitation microscopy is considered
an ideal spectroscopic method for imaging thick tissues in
vivo due to the reduced scattering of infrared radiation.
Although imaging has been reported on brain neocortex at
600–800 μm of depth, much less uniform tissues, such as
lymphonodes, are characterized by highly anisotropic light
scattering that limits the penetration length. We show that
the most severe limitation for deep imaging of lympho-
nodes appears to be the tissue scattering and the diffuse
fluorescence emission of labeled cell (lymphocytes) in
layers above the focusing plane. We report a study of the
penetration depth of the infrared radiation in a model
system and in ex vivo lymphonodes and discuss the pos-
sibility to apply Fourier filtering to the images in order to
improve the observation depth.

Keywords Non-linear spectroscopy · Fluorescence ·
Scattering

Abbreviations
TPE   Two-photon excitation
SHG   Second harmonic generation
IR   Infrared

M. Caccia · L. Sironi · M. Collini · G. Chirico (✉)
Dipartimento di Fisica, Università di Milano Bicocca,
Milan 20125, Italy
e-mail: giuseppe.chirico@mib.infn.it

I. Zanoni · F. Granucci
Dipartimento di Biotecnologie e Bioscienze,
Università di Milano Bicocca, Milan 20125, Italy

Introduction

The use of two-photon excitation (TPE) for fluorescence and
second harmonic (SHG) imaging of biological samples is
nowadays well established on a variety of systems (Bousso
2002; Cox 2003; Helmchen 2005; Mempel 2004; Salafsky
2006; Stoller 2002; Bouevitch 1993). The possibility of TPE
microscopy to perform optical tomographic imaging at
increased depths in tissues, with respect to single photon
confocal microscopy (Helmchen 2005; Cannell 1997;
Centonze 1998; Diaspro 2006) is ascribed to the low Ray-
leigh scattering of infrared (IR) radiation, since, for small
isotropic particles, the light scattering scales as the inverse
fourth power of the wavelength, $\cong \lambda^{-4}$. TPE imaging has
indeed been performed at depths $\cong 600$ μm in neocortex
samples (Helmchen 2005; Nimmerjahn 2004). However, it
must be recognized that the scattering from large anisotropic
particles decreases with a much smaller exponent, $\cong \lambda^{-2}$,
and large deformation and micro-focusing of the laser beam
are induced by micron-size objects within biological tissues.
Cells and collagen fibers are the most important sources of
the laser beam scattering (Helmchen 2005).

One of the major issues regarding deep tissue imaging is
the need to increase exponentially the excitation power
when reaching distances >50–100 μm below the specimen
surface, due to short mean free paths, $l_s \cong 20$–40 μm. Most
of the time, the full power ($\cong 1$ W) of the laser beam must be
employed when reaching hundreds of micrometers in tissues
with consequent potential photo-damage of the sample on
the focal plane (Diaspro 2006; Chirico 2003; Patterson
2000). In fact, the chromophore photo-bleaching and the cell
or tissue photo-damage is largely limited under TPE exci-
tation only in out-of-focus planes (Denk 1995; So 2000).

Due to these considerations, the first requirement to be
satisfied in order to obtain sensible results in biological and

medical experiments (Squirrel 1999; Mueller 2003) is the optimization of the excitation and detection efficiency, since it allows to minimize the photo-damage, to extend the observation time and to reach deeper planes in the tissue. One method to obtain larger sensitivity is to detect the emitted fluorescence directly above the exit pupil of the microscope objective by means of large area detectors (Centonze 1998; Majewska 2000; Nikolenko 2003; Zipfel 2003) in the so called non-descanned acquisition mode. Few non-descanned setups have been described in the literature (Zipfel 2003; Majewska 2000; Nikolenko 2003), and the details of the hardware modification of the microscope have not been reported. Moreover, the studies devoted to the characterization and improvement of the penetration depth of the IR radiation in biological tissues have been more devoted to the physics of the two-photon excitation (Beaurepaire 2001; Theer 2003) than to the specificity of the biological sample. Several groups (Helmchen 2005; Theer 2003; Mueller 2003) have reported the increase of the penetration depth when decreasing the laser repetition rate (at constant average power) and shortening the pulse width.

The main aim of this report is to study the effect of large tissue scattering on the excitation efficiency, the consequent need to use exponentially increasing excitation powers with the penetration depth and the degrading effect of the increased laser excitation power on the image signal/noise ratio. The main result of the report is to show how to partially restore the S/N on the images acquired at large (100–200 μm) depth in the tissue by Fourier filtering the images. This method should then be used, in addition to pulse energy optimization and non-descanned acquisition optics, in order to get tissue images at large penetration depths. With this purpose only, we also briefly review the design of a non-descanned detection unit applied to a commercial microscope adapted for IR excitation (BX51+FV-300, Olympus, Japan). The study presented here is performed on model and biological systems with large photon scattering. The difficulty in the imaging of deep planes in these specimens is characterized in terms of the attenuation of the excitation intensity and of the reduction of the image S/N ratio. The results indicate that the use of increased excitation power with the observation depth induces limitations of TPE microscopy for deep imaging in highly scattering media, which can be reduced by treating the images with band pass Fourier filters.

Experimental (Materials and methods)

Lymphonodes preparation

The mouse popliteal lymph node images were taken during experiments on 5 weeks old, live C57BL/6 mice kept in specific pathogen-free conditions. The mice were injected i.v., 2–3 days before the experiment, with natural killer (NK) cells labeled with 5-chloromethyl-fluorescein diacetate green tracker (CMFDA, $C_{32}H_{28}ClN_3O_4$, Molecular Probes) and T cells labeled with 4-chloromethyl benzoyl amino tetramethylrhodamine red (orange) tracker (CMTMR, $C_{25}H_{17}ClO_7$, Molecular Probes) in order to distinguish the cells from the auto-fluorescence of the biological tissue.

Turbid samples

For the investigation of the effect of the sample thickness and turbidity on the capability of the TPE microscope to image deep planes, we observed fluorescent microspheres (2.8 μm Fluorbrite[TM] Plain YG Microspheres, Tebu-Bio) in agarose gels imbued with milk.

Optical setup

The laser source was a mode-locked Ti:sapphire laser (Mai Tai HP, Spectra Physics, CA) with pulses of 120 fs full width at half maximum and 80 MHz repetition frequency. The optical setup was built around a confocal scanning head (FV-300, Olympus, Japan) mounted on an upright optical microscope (BX51, Olympus, Japan) equipped with a high working distance objective (NA = 0.95, wd = 2 mm, 20X, water immersion, XLUMPlan FI, Olympus, Japan). Non-confocal TPE imaging was performed through the FV-300 scanning unit after removing the largest pinhole from the pinhole wheel. The objective simultaneously focused the laser beam on the sample and collected the signal in epi-fluorescence geometry through either the descanned (FV-300) or the non-descanned (described hereafter) collection channels.

Non-descanned detection system design

The Non-descanned detection system (ND-unit) was designed to be mounted at right angle with respect to the BX51 dichroic splitter wheel (Fig. 1a), just above the entrance pupil of the objective lens. The detection unit had a 2 in. cylindrical connector that can be easily adapted to different microscopes. For coupling of the ND-unit to the BX51 Olympus microscope, a 2 in. hole was drilled on the microscope structure at the height of the dichroic splitter wheel (Fig. 1b, c). In order to reflect the emission light off to the ND-unit, a dichroic splitter (DF in Fig. 1a) was mounted in this wheel, contrary to that done in the usual descanned acquisition. This dichroic splitter was mounted at right angle with respect to the direction used for the epifluorescence acquisition, by adding to the Olympus cube a second dovetail rail at right angle with that provided by the producer (Fig. 1a).
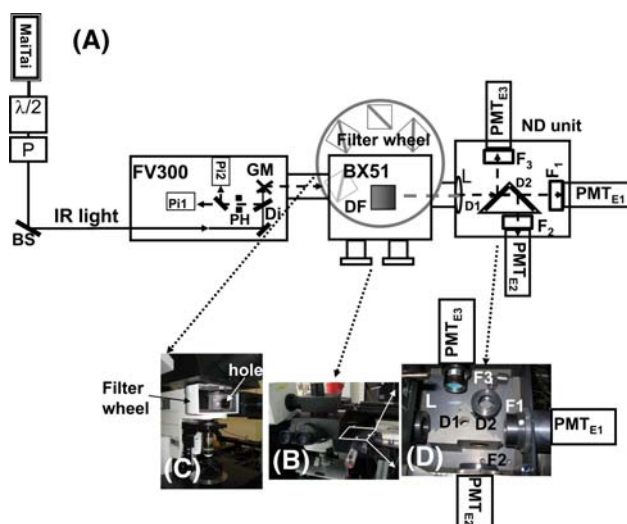
Fig. 1 a Main optical path. The laser beam passes through a $\lambda/2$ waveplate and a polarizer (*P*) and it is sent to the FV-300 scanning unit by means of a beam steering (*BS*). The light is sent through the galvo-mirrors (*GM*) to the BX51 frame (*BX51*). For descanned mode the fluorescence is discriminated by an internal dichroic (*Di*) and sent to the internal photomultipliers (*Pi1*, *Pi2*) passing through the pinhole wheel (*PH*) in which the largest pinhole has been removed in order to allow non-confocal two-photon microscopy. The filter wheel and the modified dichroic cube holder with the internal dichroic (*DF*) are indicated. For non-descanned unit, the light path is detailed: the fluorescence is steered to the ND unit, which is connected to the filter wheel by a hole drilled in the microscope structure, by the dichroic splitter (*DF*) and collimated by the collection lens (*L*) to the external photomultipliers (*PMT_{E1}*, *PMT_{E2}*, *PMT_{E3}*). The SHG and the fluorescence signals are discriminated by two external dichroic splitters (*D1*, *D2*) and by suitable band pass filters (*F1*, *F2*, *F3*). **b** The ND-unit mounted on the side of the BX51 microscope dichroic filters wheel. Panel **c** BX51 filter wheel holder with details of the modification of the microscope structure. Panel **d** Picture of the ND-unit showing the triangular-shaped mounting that hosts the dichroic filters and the cylindrical mounts for the pass band filters mounted in front of the PMTs. Fluorescence is entering as indicated by the *arrow* and the three PMT housings are visible

The ND-unit collected the emitted light right above the microscope objective lens, thereby avoiding the complex optical path back to the photomultipliers in the FV-300 scanning head. However, in order to maximize the collection efficiency from highly scattering media, the signal coming from the objective lens must be collected by a $f = 100$ mm bispherical lens (L in Fig. 1a, d). The signal reaching the ND-unit could be split into three channels by two dichroic beam splitters (D1, D2 in Fig. 1a, d), 490DCX and 540DCX (Chroma Technology Corporation, Rockingham VT, USA) and fed to three Hamamatsu analog output photomultipliers (HC125-02, Hamammatsu, Japan, PMT_{E1}, PMT_{E2}, PMT_{E3} in Fig. 1a, d) whose 21 mm (diameter) photocathodes ensured the collection of most of the light during scanning. The ND unit has been designed to minimize the distance between the entrance pupil of the objective and the active area of the detector.

The fluorescence signal was filtered by a short-pass 670 nm filter (Chroma Inc., Brattelboro, VT, USA) and by band-pass filters (F1, F2, F3 in Fig. 1a, d) in order to remove most of the residual signal due to either first harmonic scattering or to undesired auto-fluorescence from the sample. During the optical scanning of the sample (by means of the FV-300 galvo-mirros), the HC125-02 photocathode was filled for about 80% of the sensitive area. The microscope objective lens used here, magnification $20\times$, NA = 0.95 and high working distance (2 mm), coupled with the non-descanned unit allowed the imaging of fields of view $\cong$ 460 μm × 460 μm. The pre-amplified output of the HC125-02 photomultipliers (hereby referred to as external PMTs) is 0–3 V on 50 Ω input impedance, fully compatible with the Olympus scanning controller (Majewska 2000; Nikolenko 2003). The gain of the external photomultipliers was varied by feeding a low DC voltage signal (0.35–12.5 V) to the control pin of the Hamamatsu HC125 PMT. The fluorescence and SHG signals could then be processed by means of the Fluoview 5.0 software (Olympus, Japan) irrespective of the excitation mode (single confocal excitation or TPE) and the detection path (internal FV300 or external non-descanned). Images shown in the results are typically the result of 5 or 10 kalman average scans with 10 μs of residence time per pixel.

Data acquisition and analysis

The laser excitation power on the focal plane was varied between the range 1 and 120 mW, similarly to previous studies (Campagnola 2002; Plotnikov 2006). No appreciable photobleaching of the samples was detected during the whole duration of the measurements and the excitation power could be further reduced when using the ND-unit.

The evaluation of the signal and the noise levels on the images were accomplished by computing an average of at least five different regions of interest (ROIs) taken from the bright (<S>) and the dim (<N>) regions of the same image. For image filtering (convolution and Fourier high pass filters), the ImageJ software (1.37 v, W. Rasband, National Insitutes of Health, USA, http://rsb.info.nih.gov(ij/) was used.

Results and discussion

Microscope optical characterization

We characterized the performance of the microscope on transparent samples, both in the descanned and the non-descanned acquisition modes, and found that the ND-unit allows an increase of $\cong$10 times in the image S/N. We therefore analyzed the imaging performance of the TPE

microscope on thick, anisotropic and turbid media, such as lymphonodes, focusing on the non-descanned acquisition mode.

S/N versus turbidity and penetration depth

TPE and SHG imaging are best suited for investigating turbid samples and biological tissues in which light scattering is substantial (Hemlchen 2005; Cannell 1997; Diaspro 2006; Nimmerjahn 2004; Hemlchen 1999). Photon scattering is characterized by the mean free path l_s between two consecutive scattering events (Helmchen 2005), and affects both the excitation and collection efficiency. The collection efficiency drops substantially (corresponding to the layers closest to the tissue surface) when focusing at depths $\cong 3$ l_s (Beaurepaire 2001). This rapid decrease with the depth in the sample is due to the limited solid angle collected by the detector: one should therefore minimize the distance between the detector and the objective lens or adopt a collecting lens in the collection optics as done here. Typical values of $l_s = 100$–200 µm have been reported for brain (Taddeucci 1996; Yaroslavsky 2002).

Regarding the excitation efficiency, only the ballistic photons determine the two-photon absorption probability (Helmchen 2005; Centonze 1998). The excitation efficiency in thick turbid samples can be improved by employing higher pulse energies (Beaurepaire 2001) or shorter laser pulse width (Mueller 2003). Both methods result in a higher peak intensity and allow reaching a depth $\cong 800$ µm to 1 mm in brain and kidney tissues (Theer 2003). In order to reach larger depths with good S/N ratios in lymphonodes, characterized by much shorter l_s values, we consider alternative possibilities based on image filtering that can be adopted in addition to the increase in the pulse peak intensity (Bousso 2002; Bousso 2004; Cahalan 2003).

Our queries regard the following points. Is it the increase in the peak power the only and best suited strategy to increase efficiency and the S/N ratio in deep planes of lymphonodes? Is the axial resolution and/or the laser pulse width affected by the penetration in the tissue? In order to answer these questions, we made a characterization of the performance of the ND detection unit in model turbid media and in lymphonodes.

Figure 2a reports images taken at increasing penetration depths (0–300 µm) from the surface of the sample, on a model system composed of fluorescent microspheres (2.8 µm in diameter) diluted in milk ($l_s \cong 50$ µm) and trapped in agarose gels. The micro-beads in the agarose matrix are themselves the source of inhomogeneity. A similar situation is encountered when a large concentration of stained cells is present in a lymphonode.

For pure milk samples, the scattering path was $l_s \cong 40 \pm 4$ µm, as measured from the turbidity of a

150 µm thick sample of milk. The analysis of the images of micro-spheres embedded in agarose indicates that despite the collection of the fluorescence through a highly turbid medium (pure milk in the agarose matrix), both the radial and the axial resolutions are not largely affected as also reported elsewhere (Centonze and White 1998). The decrease of the average fluorescence signal collected from the micro-spheres in pure milk, at constant excitation power, is well described by an exponential function:

$$I \approx \exp\left[-2z/l_s\right] \tag{1}$$

in the whole range of depths explored (0–300 µm, Fig. 2a, plot, solid lines). At $z > 100$ µm, the value $l_s = 25 \pm 5$ µm is measured (Fig. 2a, plot, dashed lines) independent of the excitation power used (different symbols in Fig. 2a, plot) and in good agreement with the mean scattering path of the photons $l_s \cong 40 \pm 4$ µm. This indicates that the collection efficiency of the ND unit does not largely affect the penetration depth: the collection lens in the detection unit is sufficiently close to the objective to ensure the collection of a substantial fraction of the solid angle, a condition particularly important when the objective lens collects light from a diffuse source (Beaurepaire 2001).

In order to overcome the exponential decrease in the excitation efficiency with the penetration depth (Fig. 2a, plot), the excitation power must be increased while imaging deeper in the scattering sample. By doing so, not only the background fluorescence increases, but also large diffuse structures in the images appear on deep planes images (see images in Fig. 2a). This is a combined effect of the increased excitation intensity and the non-linearity of the TPE signal. The power in the focal plane decays exponentially with the depth z as (Helmchen 2005):

$$P_{\text{ball}}(z) = P_0 \exp\left(-\frac{z}{l_s}\right) \tag{2}$$

where P_0 is the surface power and l_s is the scattering length. As verified for samples in pure milk, the fluorescence signal changes exponentially with a decay length $d \cong l_s/2$. Equation 2 implies that the experimental value of the excitation power must increase with the focusing depth z as:

$$P_{\text{exp}}(z) \cong P_0 \exp\left(+\frac{2z}{l_s}\right). \tag{3}$$

A fluorescent object residing at position $z-\varepsilon$ will then be excited by the intensity

$$\tilde{I}(z,\varepsilon) = \frac{P_{\text{exp}}(z)}{w_0^2\left(1+\left(\frac{\varepsilon}{z_R}\right)^2\right)} \tag{4}$$

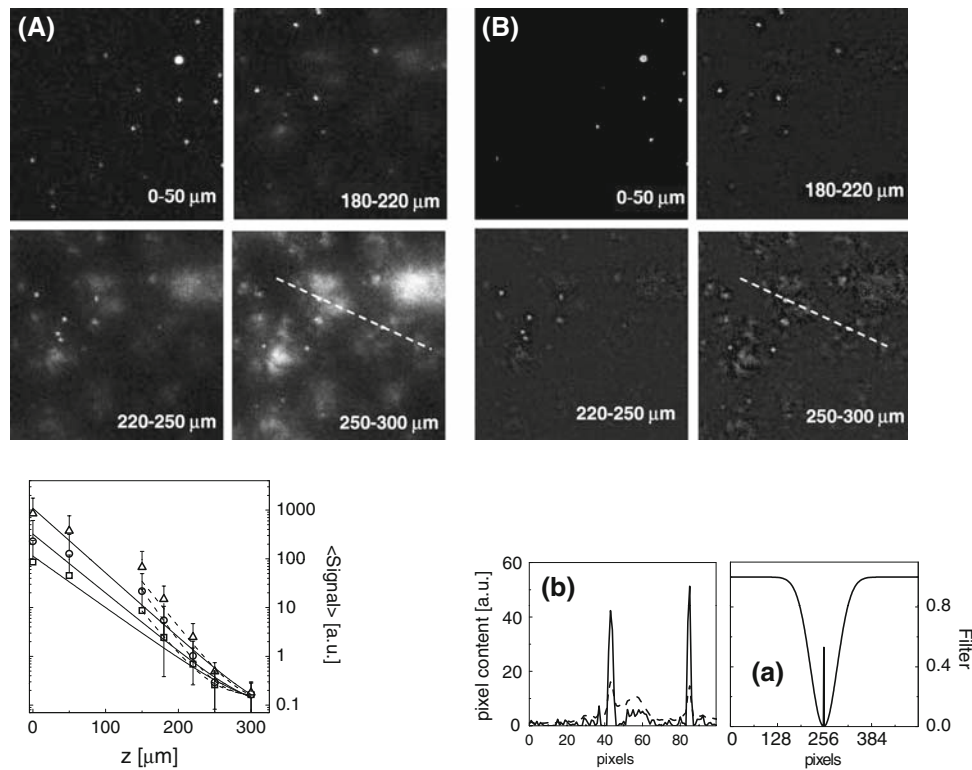when the microscope is focused at depth z, while it experiences an intensity

Fig. 2 A Z-projection of 25 stacks collected from a sample of 2.8 μm diameter fluorescent beads in milk (agarose matrix) at increasing depth in the sample. The excitation power varied as $P = 1.6$ mW (0–50 μm); $P = 23$ mW (180–220 μm); $P = 52$ mW (220–250 μm); $P = 109$ mW (250–300 μm). The contrast of the images was varied for display. Field of view = 177×177 μm². The plot reports the average signal of the beads on each Z-projection versus the average depth. *Solid* and *dashed* lines are exponential best fit to the data as discussed in the text. *Different symbols* refer to different excitation power of the laser: *triangles* (60 mW), *circles* (20 mW), *squares* (10 mW). **B** The same images as in panel (**A**), filtered by a low pass FFT filter for objects less than 5 μm in diameter. A section of the filter along the radial direction is displayed in the plot (**a**). The plot (**b**) represents the profile of the images taken on the stack 250–300 μm along the *dashed line* shown in the corresponding images. The *dashed* and the *solid lines* correspond to the unfiltered and filtered images, respectively. The profile taken on the unfiltered image has been multiplied by a factor 4 for display purposes

$$\tilde{I}(z - \varepsilon, 0) = \frac{P_{\exp}(z - \varepsilon)}{w_0^2} \qquad (5)$$

when the microscope is focused at the depth $z - \varepsilon$. In Eqs. 4 and 5, w_0 is the beam waist, which is assumed to be constant with depth (no apparent increase in the resolution with z is observed) and z_R is the Rayleigh range $z_R = \pi w_0^2 / \lambda$. According to Eqs. 4 and 5, we may have similar excitation intensity values on an object residing on a plane at distance ε from the focal plane and on a similar object residing at the focal plane if:

$$\exp\left[-2\frac{\varepsilon}{l_s}\right] = \frac{1}{\left(1 + \left(\frac{\varepsilon}{z_R}\right)^2\right)} \qquad (6)$$

or

$$2\frac{\varepsilon}{l_s} = \ln\left[1 + \left(\frac{\varepsilon}{z_R}\right)^2\right] \qquad (7)$$

In this case, the overall fluorescence signal from out of focus planes become comparable with that collected from the focal plane, although the first leads to blurred and non-resolved images. For an NA = 0.9 objective, we estimate $w_0 \cong 0.8$ μm for $\lambda = 0.9$ μm and $z_R \cong 2.3$ μm. In this case, Eq. 7 has a solution for $\varepsilon \cong 0.4$ μm, definitely within the point spread function width along the optical path. However, the objective lenses are seldom used at the maximum aperture in excitation. This is due to the difficulty to obtain a uniform illumination field while scanning the sample with the light beam. If the numerical aperture effectively used for excitation is NA $\cong 0.5$, the solution to Eq. 7 becomes $\varepsilon \cong 4.5$ μm. This simple estimate suggests that the blurred defocused structures in the images (Fig. 2a) coming from out of focus planes could be reduced experimentally (with an increase in the S/N on the image) more efficiently by employing larger numerical apertures in excitation than by merely increasing the peak excitation intensity on the focal plane.

Image filtering

The fluorescent objects, microspheres in the model systems and lymphocytes in the lymphonodes, are still present above the image background, as can be seen, for example, in the images of micro-beads in pure milk lying at depths $\cong 250$–300 μm (Fig. 2A). We have therefore verified the possibility to apply a Fourier filter to these images in order to bring into evidence the presence of objects of the expected size, about 3 μm in this case, actually very close to the size of most cells.

The Fourier filter has been applied to stacks of 14–16 slices taken with $\Delta z \cong 1.3$ μm and tested on micro-beads embedded in agarose gel and milk. The projection was performed by assigning at each pixel the maximum value of the whole stack. Then a band pass FFT filter, whose spectrum is reported in Fig. 2B (a), was applied to the resulting projection image to reject objects above 5 μm in diameter. In this way, bright spots of the size expected for the micro-spheres (Fig. 2B) became clearly visible also on deep planes. When the objects in the images are all very similar in size, as in the present cases, the exact value of the size threshold in the FFT filter and the type of stack

projection (maximum value, sum or average) does not critically affect the result of the image processing (data not shown).

Apart from the visual effect on the image, also the signal/noise ratio increases substantially when applying the Fourier filter, as shown in Fig. 2B (b). Similar results were obtained on lymphonodes stained with fluorescent lymphocytes (Fig. 3). In this case, each image of the stack is acquired on the blue (SHG) and the green (lymphocytes) channels and summed in a unique black and white image. The application of the FFT filter does not decrease the possibility of detecting the collagen fibers (Fig. 3) that provide the estimate of the outer size of the lymphonode.

It must be noticed that the filtering procedure is mostly necessary and effective when the scattering of the medium is large and the concentration of the bright objects is high. In such conditions, in fact, we need to use higher and higher excitation intensity when taking images on deep plane into the sample: the above lying objects then induce large blurring effects on the images (Figs. 2A, 4). In agreement with this expectation, we can see that the effect of the FFT filter is limited when it is applied to images of lymphocytes at low concentration in lymphonodes, as

Fig. 3 Raw images (left column) and FFT filtered images (middle column) of stained lymphocytes in lymphonodes. Each image (350 μm × 350 μm) is a projection of a stack taken between 60 and 80 μm (a), 80 and 100 μm (b) and 100 and 120 μm (c). Right column: RGB merge of FFT-filtered images of stained lymphocytes in ex-vivo samples of mouse lymphonodes. a The RGB colors correspond to the z-projection of the stacks from 0 to 30 μm (blue), from 30 to 60 μm (green) and from 60 to 80 μm (red). b The RGB colors correspond to the Z-projection of the stacks from 30 to 60 μm (blue), from 60 to 80 μm (green) and from 80 to 100 μm (red). c The RGB colors correspond to the Z-projection of the stacks from 60 to 80 μm (blue), from 80 to 100 μm (green) and from 100 to 120 μm (red)
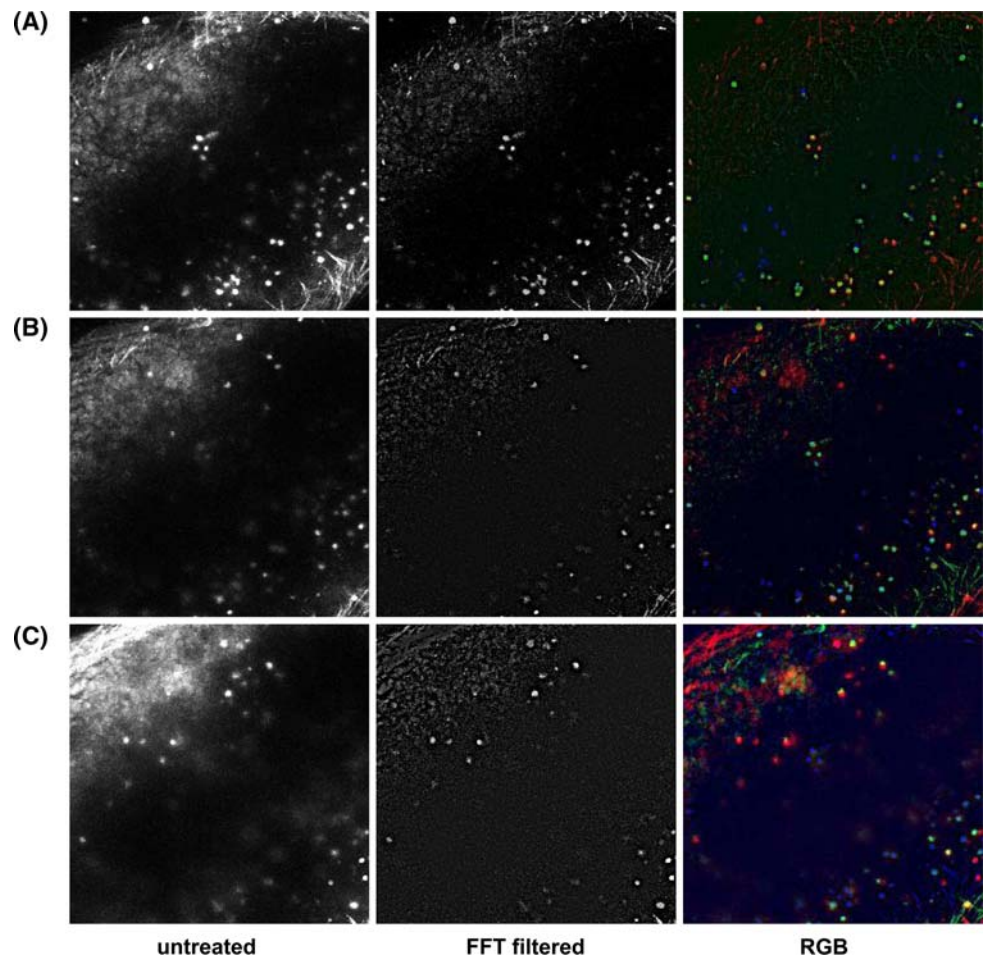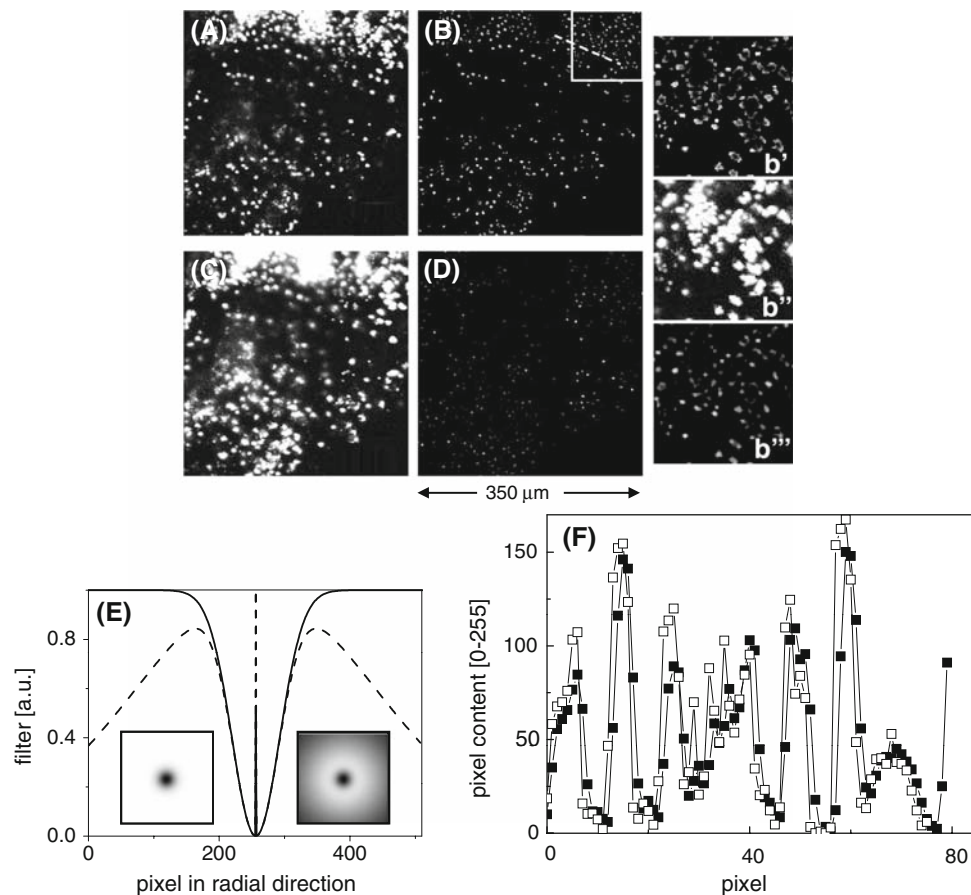
Fig. 4 Analysis of lymphonodes stained with fluorescent micro-beads. **a** Projection of stacks taken between 40 and 60 μm below the lymphonode cortex. **b** FFT filtered image of image (**a**) with the filter shown as *solid line* in the panel (**e**). **c** Projection of stacks taken between 60 and 80 μm below the lymphonode cortex. **d** FFT filtered image of image (**c**). The plot in panel (**e**) shows two FFT filters used: the *dashed line* corresponds to a slight smoothing on the image. The images in this plot display the filters shown in terms of the radial coordinate in the plot itself. The plot in the panel (**f**) shows the pixel content along the *dashed line* in the image (**b**) when the image (**a**) is treated with the two FFT filters shown in the panel (**e**): *open* and *closed squares* in this plot correspond to the filters shown as *solid* and *dashed lines* in panel (e). The images in the panels (*b'*), (*b''*) and (*b'''*) are zoomed images of the square reported in the image (**b**): image (*b''*) is the unfiltered zoom, image (*b'*) and image (*b'''*) are filtered with the FFT filters shown as *solid* and *dashed lines* in panel (**e**), respectively

reported in Fig. 3. In contrast, if we take the images of fluorescent micro-beads injected at high concentration in lymphonodes (Fig. 4), we observe large blurred objects (Fig. 4a, c) whose effect is largely diminished after applying the FFT filtering procedure (Fig. 4b, d). In such extreme cases, the choice of the shape of the FFT filter may help in further improving the image quality and S/N ratio while minimizing the high spatial frequency noise that arises from the filter application.

As an example, an FFT filter with a slight smoothing character (Fig. 4e, dashed line), applied to the images of micro-beads in lymphonodes, produces slightly smaller S/N ratios (Fig. 4f) than those obtained by applying the flat FFT filter used above (Fig. 4e, solid line). The smoothing FFT filter (Fig. 4e, dashed line), however, produces images with a smaller contribution of high spatial frequency artifacts, as can be seen from the zoomed images reported in

Fig. 4b''' (FFT filter + smoothing, dashed line in Fig. 4e), compared to the images in Fig. 4b'' (unfiltered) and in Fig. 4b' (FFT filter, solid line in Fig. 4e). Actually, the best choice of the filter to be used must take into account the scattering level of the tissue, the concentration and the brightness of the searched objects (cells), and cannot therefore be generalized. The filtering of the large blurred spots produces a dramatic reduction of the intensity and S/N ratio of these unwanted structures in the images, leaving however dim haloes (Fig. 4b') or spots (Fig. 4b'''). It is then possible to discriminate between the searched objects (cells or microspheres in these examples) and the artifacts by means of a suitable threshold on the images.

When trying to follow the distribution and the dynamics of cells deep within the lymphonodes, it is crucial to discern cells lying on different planes. The question is whether the effective axial resolution is affected by the

penetration of the light in the lymphatic tissue. Also, this issue is related to the need to increase the excitation power with the depth in the tissue according to $\cong \exp(+2z/l_s)$. In fact, in most of the images the cells (or the microspheres) appear saturated and this implies an apparently larger width of their axial image. When taking into account this effect, the axial resolution is very close to the value measured in highly transparent media (spheres embedded in agarose gels without milk). From the experimental point of view, however, we need to discern cells that lie in different planes along the optical path also when using high excitation intensity. The FFT filtering algorithm adopted above provides an efficient way to overcome this problem. We projected stacks $\cong 20$ μm in thickness, applied a FFT filter and a threshold and merged adjacent triples or couples of them in RGB or RG images in order to bring into evidence any superposition of cells detected on adjacent stacks. From Fig. 3, one can see that still at a depth $\cong 120$ μm in lymphonodes, different cells could be discerned in adjacent stacks. For microspheres in agarose gels imbued with milk, this value rises to $\cong 250$ μm, as can be seen from the images reported in Fig. 4b, d. Since the scattering length l_s in pure milk and lymphonodes is respectively 40 and 20 μm at 800 nm excitation wavelength, the simple image filtering method presented here allows in reaching a depth of $\cong 6\ l_s$ with reasonable S/N ratios, without complex and expensive technical improvements of the laser and microscope setup, which would in any case further and substantially improve the penetration depth of the non-linear microscope.

Conclusions

The physical principles of non-linear excitation allow collecting fluorescence and SHG signals in vivo with enhanced S/N ratio at reduced values of the excitation intensity, therefore minimizing damages to the biological tissues. This has been widely reported in recent years mainly for brain. However, this general statement must be tailored to the specific tissue to be studied. When large and anisotropic scattering is present in the sample, particular care must be given to a number of technical improvements of the non-linear microscope and the image analysis. The results discussed here indicate that, besides the optimization of the collection and of the excitation efficiency, careful image analysis should be performed. In fact, the increase in the excitation power when imaging planes lying deep in the tissue implies the increase in the fluorescence background that originates from the tissue itself. This may be overcome, at least partially, by FFT filtering the images with band pass filters. The exact choice of the shape of the filter appears to be related to the amount of tissue scattering

and the concentration of the fluorescent objects in the tissue.

References

Beaurepaire E, Oheim M, Mertz J (2001) Ultra-deep two-photon fluorescence excitation in turbid media. Opt Commun 188:25–29

Bouevitch O, Lewis A, Pinevsky I, Wuskell JP, Loew LM (1993) Probing membrane potential with non-linear optics. Biophys J 65(2):672–679

Bousso P, Bhakta NR, Lewis RS, Robey E (2002) Dynamics of thymocyte–stromal cell interactions visualized by two-photon microscopy. Science 296(5574):1876–1880

Bousso P, Robey EA (2004) Dynamic behavior of T cells and thymocytes in lymphoid organs as revealed by two-photon microscopy. Immunity 21:349–355

Cahalan MD, Parker I, Wei SH, Miller MJ (2003) Real-time imaging of lymphocytes in vivo. Curr Opin Immunol 15:372–377

Campagnola PJ, Millard AC, Terasaki M, Hoppe PE, Malone CJ, Mohler WA (2002) Three-dimensional high-resolution second harmonic generation imaging of endogenous structural proteins in biological tissues. Biophys J 81:493–508

Cannell MB, Soeller C (1997) High resolution imaging using confocal and two-photon molecular excitation microscopy. Proc R Microsc Soc 32:3–8

Centonze VE, White JG (1998) Multiphoton excitation provides optical sections from deeper within scattering specimens than confocal imaging. Biophys J 75:2015–2024

Chirico G, Cannone F, Baldini G, Diaspro A (2003) Two-photon thermal bleaching of single fluorescent molecules. Biophys J 84(1):588–598

Cox G, Kable E, Jones A, Fraser I, Manconi F, Gorrel MD (2003) 3-Dimensional imaging of collagen using second harmonic generation. J Struct Biol 141(1):53–62

Denk W, Piston DW, Webb WW (1995) Two-photon molecular excitation in laser scanning microscopy. In: Pawley JB (ed) Handbook of biological confocal microscopy. Plenum, New York, pp 445–458

Diaspro A, Chirico G, Collini M (2005) Two-photon fluorescence excitation and related techniques in biological microscopy. Quart Rev Biophys 38(2):97–166

Hemlchen F, Svoboda K, Denk W, Tanl DW (1999) In vivo dendritic calcium dynamics in deep-layer cortical pyramidal neurons. Nat Neurosci 2:989–996

Helmchen F, Denk W (2005) Deep tissue two-photon microscopy. Nat Methods 2:932–940

Majewska A, Yiu G, Yuste R (2000) A custom-made two-photon microscope and deconvolution system. Eur J Physiol 441:398–408

Mempel TR, Henrickson SE, von Andrian UH (2004) T-cell priming by dendritic cells in lymph nodes occurs in three distinct phases. Nature 427:154–159

Mueller M, Schmidt J, Mironov SL, Richter DW (2003) Construction and performances of a custom built two-photon laser scanning system. J Phys D: Appl Phys 36:1747–1757

Nikolenko V, Nemt B, Yuste R (2003) A two-photon and second harmonic microscope. Methods 30:3–15

Nimmerjahn A, Kirchoff F, Kerr JN, Hemlchen F (2004) Sulforhodamine 101 as a specific marker of astroglia in the neocortex in vivo. Nat Methods 1:31–37

Patterson GH, Piston DW (2000) Photobleaching in two-photon excitation microscopy. Biophys J 78(4):2159–2162

Plotnikov SV, Millard AC, Campagnola PJ, Mohler WA (2006) Characterization of the myosin based source for second harmonic generation from muscle sarcomeres. Biophys J 90(2): 693–703

Salafsky JS (2006) Detection of protein conformational change by optical second harmonic generation. J Chem Phys 125(7): 074701-1-7

So PTC, Dong CY, Masters BR, Berland KM (2000) Two-photon excitation fluorescence microscopy. Ann Rev Biomed Eng 2:399–429

Stoller P, Kim BM, Rubenchik AM, Reiser KM, Da Silva LB (2002) Polarization-dependent optical second harmonic imaging of a rat tail tendon. J Biomed Optics 7(2):205–214

Taddeucci A, Martelli F, Barilli M, Ferrari M, Zaccanti G (1996) Optical properties of brain tissue. J Biomed Opt 1:117–123

Theer P, Hasan MT, Denk W (2003) Two-photon imaging to a depth of 1000 μm in living brains by use of a $Ti:Al_2O_3$ regenerative amplifier. Opt Lett 28:1022–1024

Yaroslavsky A et al (2002) Optical properties of selected native and coagulated human brain tissue in vitro in the visible and infrared spectral range. Phys Med Biol 47(12):2059–2073

Zipfel WR, Williams RM, Webb WW (2003) Nonlinear magic: multiphoton microscopy in the biosciences. Nature Biotech 21(11):1369–1377